

Breaking polarization-breakdown strength paradox for ultrahigh energy storage density in NBT-based ceramics

Received: 28 October 2024

Accepted: 11 June 2025

Published online: 07 July 2025



Wenjun Cao¹, Yanwei Wu², Xiaoyu Yang², Daqin Guan³, Xuecen Huang^{1,4}, Feng Li², Youmin Guo¹, Chunchang Wang¹✉, Binghui Ge²✉, Xu Hou^{5,6}✉ & Zhenxiang Cheng⁷✉

Dielectric capacitors are crucial in contemporary electronic devices for storing and recycling electric energy. However, their energy-storage density is significantly hindered by the paradox between polarization (P) and breakdown strength (E_b). Herein, we propose a strategy to overcome the paradox through a unique high-entropy design aimed at regulating phase structure and minimizing interfacial polarization. This approach ensures an ample polar phase while providing a sufficiently high field to induce a transition from antiferroelectric to ferroelectric, significantly enhancing polarization. This strategy has been successfully applied to the $\text{Na}_{0.5}\text{Bi}_{0.5}\text{TiO}_3$ (NBT) system, modified by high-entropy material $(\text{Na}_{1/6}\text{Bi}_{1/6}\text{Ca}_{1/6}\text{Sr}_{1/6}\text{Nd}_{1/6}\text{Li}_{1/6})\text{TiO}_3$ (NBCSNLT). For the $(1-x)\text{NBT}-x\text{NBCSNLT}$ bulk ceramics, our findings indicate that E_b consistently increases with the NBCSNLT content, effectively resolving the paradox for electric field above 550 kV/cm. This leads to simultaneously high E_b and large P . Consequently, an ultrahigh recoverable energy-storage density (W_{rec}) of 18.2 J/cm^3 , a high efficiency (η) of 85.6%, and a record-breaking energy-storage potential (W_{rec}/E_b) value of 0.026 mC/cm^2 , were achieved in the bulk 0.55NBCSNLT. Additionally, this sample exhibited excellent temperature/frequency stability. This strategy provides an effective pathway for surmounting the P - E_b paradox, paving the way for ultrahigh energy-storage density.

Energy-storage ceramic capacitors are recognized as a crucial component in pulsed power devices, attributed to their ultrahigh power density, outstanding charge/discharge capability, and excellent chemical stability¹. However, a significant limitation to their practical application is their low recoverable energy density ($W_{\text{rec}} < 5 \text{ J/cm}^3$), a challenge stemming from the paradox between polarization (P) and breakdown strength (E_b). This paradox implies that achieving a high

saturation polarization (P_m) and a large breakdown field simultaneously is currently unattainable² (see Fig. S1). To achieve a significant advancement in W_{rec} , overcoming this paradox is essential. Modulating the structure, such as through the development of core-shell³ and layered structures^{4,5}, has been identified as a viable approach to simultaneously achieve large P and high E_b . Additionally, inducing an antiferroelectric (AFE) to ferroelectric (FE) phase transition through

¹Laboratory of Dielectric Functional Materials, School of Materials Science & Engineering, Anhui University, Hefei, China. ²Institute of Physical Science and Information Technology, Anhui University, Hefei, China. ³School of Mines: Minerals, Energy and Chemical Engineering, Curtin University, Perth, WA, Australia. ⁴School of Material and Chemical Engineering, Chuzhou University, Chuzhou, China. ⁵Department of Industrial and Systems Engineering, Hong Kong Polytechnic University, Hong Kong, China. ⁶The Hong Kong Polytechnic University Shenzhen Research Institute, Shenzhen, China. ⁷Institute for Superconducting and Electronic Materials, Faculty of Engineering and Information Sciences, Squires Way, University of Wollongong, North Wollongong, NSW, Australia. ✉e-mail: ccwang@ahu.edu.cn; bhge@ahu.edu; emhouxu@zju.edu.cn; cheng@uow.edu.au

external fields has been proposed as a promising strategy for accomplishing this goal⁶. Despite these strategies, the W_{rec} values attained remain unsatisfactory. This fact arises because enhancing the energy-storage performance (ESP) necessitates transforming long-range ferroelectric order into short-range polar nanoregions (PNRs). Consequently, many PNRs become irreversible due to clamping effects⁷, making it challenging to further increase polarization intensity. Achieving full polarization of PNRs requires sufficient electric fields, but the inherently high resistance of grain boundaries compared to grains means that a large portion of the voltage falls across the grain boundaries, leaving grains with relatively less voltage. This condition prevents the full polarization of the polar phase within the grains.

To intensify polarization, increasing the voltage shared by the grains is essential. This requires reducing the resistance mismatch between grain and grain boundaries, i.e., minimizing interfacial polarization⁸. Our recent findings demonstrate that a high-entropy design incorporating large bandgap oxides effectively mitigates interfacial polarization and enhances E_b ⁹. High-entropy design is therefore a promising solution to the P - E_b paradox for improved ESP. However increasing configurational entropy stabilizes non-polar cubic phase structure ($Pm3m$ space group, C-phase), which reduces polarization¹⁰ but notably increases E_b as indicated by the P - E_b paradox. With the increase of external electric field, it is difficult to ensure that a small remnant polarization (P_r) value can be maintained under high field conditions. This creates a secondary paradox between W_{rec} and efficiency (η) as seen in Fig. S1. This paradox suggests that simply increasing entropy is insufficient for ESP improvement. It is crucial to balance entropy while ensuring a sufficient polar phase.

To address these paradoxes, we proposed a targeted high-entropy design with twofold effects that can regulate phase structure and suppress interfacial polarization. This dual-effect design ensures the presence of a sufficient polar phase and provides the necessary field strength to fully polarize the material. To verify the effectiveness of the strategy, we selected $\text{Na}_{0.5}\text{Bi}_{0.5}\text{TiO}_3$ (NBT), a lead-free material with energy-storage capabilities, as base material. NBT is particularly suitable due to its coexistence of multiple phases: namely, the FE rhombohedral phase (R-phase with $R3c$ space group) and the weak AFE tetragonal phase (T-phase with $P4bm$ space group) across a wide temperature range around room temperature^{11,12}. The T-phase transforms into a ferroelectric phase at high fields, contributing to polarization. This structural feature makes NBT an ideal candidate for field-induced AFE to FE phase transitions, holding potential for enhanced polarization at high fields.

Equimolar high-entropy ceramic ($\text{Na}_{1/6}\text{Bi}_{1/6}\text{Ca}_{1/6}\text{Sr}_{1/6}\text{Nd}_{1/6}\text{Li}_{1/6}$) TiO_3 (NBCSNLT, with configurational entropy $\Delta S = 1.79 R$) was used as a dopant to adjust both phase structure and interfacial polarization of NBT. NBCSNLT was chosen for the key reasons: (1) NBCSNLT-induced positional fluctuations can disrupt long-range ferroelectric macrodomains, promote the formation of short-range ordered PNRs, thereby regulating the phase structure and ensuring a sufficient T-phase. (2) It comprises a series of wide-band-gap linear ceramics, such as SrTiO_3 (3.2 eV¹³), CaTiO_3 (3.8 eV¹⁴), and Nd_2O_3 (5.05 eV¹⁵). They act as insulating additives to enhance grain resistance and reduce the resistance mismatch between grains and grain boundaries, thereby suppressing interfacial polarization and ensuring a sufficiently high E_b .

Lead-free ceramics of $(1-x)\text{Na}_{0.5}\text{Bi}_{0.5}\text{TiO}_3 \cdot x(\text{Na}_{1/6}\text{Bi}_{1/6}\text{Ca}_{1/6}\text{Sr}_{1/6}\text{Nd}_{1/6}\text{Li}_{1/6})\text{TiO}_3$ (NBT- x NBCSNLT, where $x = 0, 0.25, 0.35, 0.45, 0.5, 0.55, 0.6$, and 0.65) were designed and prepared via solid-state reaction method. Investigations on energy-storage properties reveal that E_b increases continuously with the increase of NBCSNLT content. The P - E_b paradox is pronounced within the range of $x \leq 0.45$. However, for $x > 0.45$, the paradox is successfully overcome, resulting in an excellent ESP ($W_{\text{rec}} = 18.2 \text{ J/cm}^3$ and $\eta = 85.6\%$) in the 0.55NBCSNLT sample. This achievement marks a significant advancement in addressing the P - E_b paradox and achieving ESP.

Results and discussion

Bandgap and phase structure of the x NBCSNLT ceramics

The ΔS value as a function of the NBCSNLT content (x) is depicted in Fig. S2. ΔS monotonically increases from $0.69 R$ for pure NBT to $1.68 R$ for the sample with 0.65NBCSNLT. Fig. 1a illustrates the atomic disorder and lattice distortion caused by differences in atomic size, mass, and electronegativity as foreign atoms are introduced into equivalent sites. These atomic disorder and lattice distortion strongly hinder the transmission of electrons, thereby intrinsically increasing the breakdown strength. Due to the close relationship between E_b and bandgap (E_g), the Vienna ab initio simulation package (VASP) in the projector enhanced wave (PAW) method¹⁶ was used to discuss the E_g differences between different phases. Crystal structures of the $R3c$, $P4bm$, and $Pm3m$ phases used for the calculations were illustrated in Fig. S3, the calculated results of $R3c$ phases of NBT ceramic were selected to show in Fig. S4. The calculated results of $R3c$, $P4bm$, and $Pm3m$ phases of 0.55NBCSNLT were shown in Fig. 1b–d and S5. The results reveal that E_g increases monotonically from 2.97 eV for pure NBT to 3.18 eV for 0.65NBCSNLT (Fig. S6). This increase can be attributed to the incorporation of wide bandgap oxides and high-entropy-induced disorder, which enhances the insulation properties of the samples¹⁷. To verify the rationality of the calculation results, the UV absorption spectroscopy was used to measure the E_g value. The UV-vis absorption spectra, as shown in Fig. S7, clearly show that E_g increases from 2.97 to 3.18 eV with increasing NBCSNLT content. Our simulation agrees well with the experimental result, confirming that our high-entropy design can effectively increase E_b value, which is crucial for superior ESP.

The phase structure studied by XRD (Fig. 1e) reveals that all the samples exhibit single pseudo-cubic perovskite structure with no detectable secondary phases. This result is consistent with previous reports^{18,19}, indicating that Na^+ , Li^+ , Sr^{2+} , Ca^{2+} , Nd^{3+} , and Bi^{3+} ions completely enter the lattice of the bismuth titanate to form a solid solution. Similar to previous finding^{20,21}, the (200) peak appears as a single peak (Fig. S8a), suggesting that the polyphase of $R(R3c)$, $T(P4bm)$, and $C(Pm3m)$ coexist in the sample. The Rietveld refinements of the XRD patterns reveal that the pure NBT sample ($x = 0$), NBCSNLT-modulated samples with $0 < x < 0.50$, $0.50 \leq x \leq 0.55$ and $x \geq 0.60$ can be well fitted by a single $R3c$, $R3c + P4bm$, $R3c + P4bm + Pm3m$ and $P4bm + Pm3m$ space groups, respectively (Figs. 1f, S9). The refined parameters are displayed in Table S1. The indicators of refinement quality, R_p , and R_{wp} are less than 10%, and the fitted curves are in good agreement with the experimental data, indicating that the refinement results are satisfactory and reliable. Additionally, the multiphase nature of the 0.55NBCSNLT sample is further confirmed by synchrotron XRD result recorded at room temperature, as the pattern can be well fitted by $R3c + P4bm + Pm3m$ space groups (Fig. S10). The deduced proportions of $R3c$, $P4bm$, and $Pm3m$ phases with the NBCSNLT doping level are shown in Fig. S8b, which clearly evidences that the high-entropy design endows the NBCSNLT-modulated samples with multiphase.

Local phase structure of the NBT and 0.55NBCSNLT samples

To further confirm the presence of multiphase, transmission electron microscope (TEM) observations were conducted on the NBT and 0.55NBCSNLT samples. The bright-field TEM allows for a more intuitive observation of the domain sizes of the pure NBT sample, as shown in Fig. 2a, where large stripe domains can be clearly observed. Whereas the lamellar streak domain structure for the 0.55NBCSNLT sample (Fig. 2b) is invisible, indicating a much smaller domain size. This fact demonstrates that entropy increase can effectively reduce the domain size. The selected area electron diffraction (SAED) patterns taken from the white squares in Fig. 2a along $[110]c$ and Fig. 2b along $[110]c$ and $[111]c$ are shown as insets in corresponding figures. According to previous reports^{22–25}, the $R3c$ and $P4bm$ phases are characterized by the tilting of the inverted a^0a^0 oxygen octahedron and in-phase $\text{a}^0\text{a}^0\text{c}^+$

oxygen octahedron, respectively. The $1/2(000)$ superlattice points, as shown in the insets of Fig. 2a, b with one of them indicated by a red circle, match the $R3c$ symmetry²⁴. The $1/2(00e)$ superlattice points, as shown in the inset of Fig. 2b with one of them indicated by a red circle, match the $P4bm$ symmetry²⁵. The TEM results further confirm the XRD refinement results that the pure $R3c$ phase in NBT is transformed into the $R3c$, $P4bm$, and $Pm3m$ phases in 0.55NBCSNLT by our high-entropy design. A pertinent question is, however, why the C phase cannot be revealed by the TEM observation? This is because that the $Pm3m$ space group exhibits no superlattice points⁸.

Given that the resolution of conventional TEM does not allow further exploration of the phase structure observed in the

0.55NBCSNLT sample, so we applied atomically resolved high-resolution high-angle annular dark-field scanning transmission electron microscope (HAADF-STEM) images to directly observe the atomic-level structure of the 0.55NBCSNLT sample²⁶. As shown in Fig. 2c, d, the positions of atomic columns were estimated using 2D Gaussian fitting, where the arrows indicate the direction and magnitude of the atomic displacements^{27–29}. The polarization vectors were quantitatively determined by applying two-dimensional Gaussian fitting to refine atomic column positions, with the vectorial relationships defined as displacement vectors originating from the centroid of B-site cation clusters to adjacent A-site cation coordinates, as indicated by the arrows in Fig. 2c, d. The R and T phases can be directly identified by

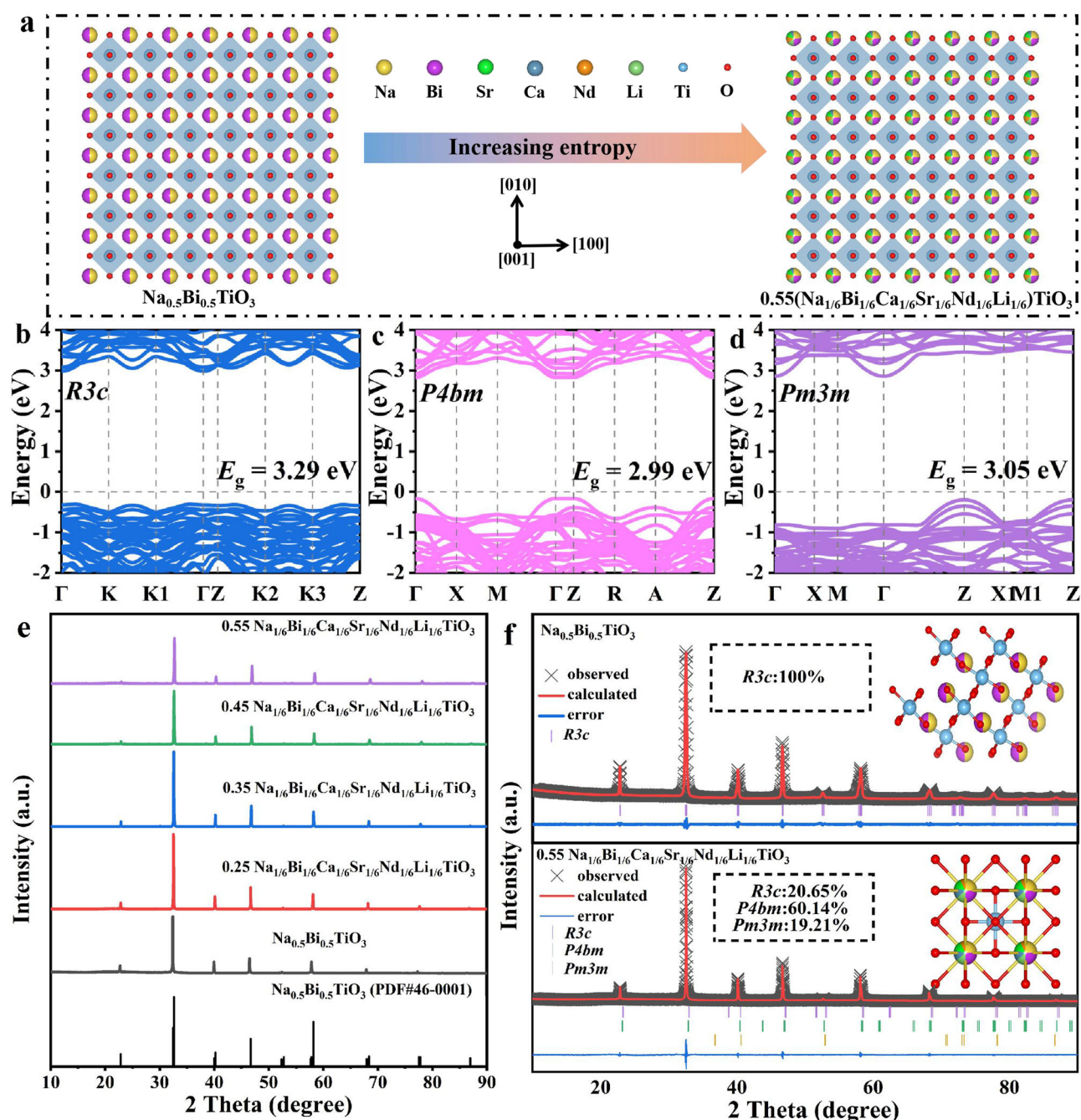


Fig. 1 | Bandgap and phase structure of the x NBCSNLT ceramics. a Schematic diagram of the atomic disorder and lattice distortion with increasing entropy in a perovskite structure. **b** Band structures of 0.55NBCSNLT with R phase ($R3c$), **c** T

phase ($P4bm$), and **d** C phase ($Pm3m$). **e** XRD patterns of the x NBCSNLT. **f** Rietveld refinement results of $x = 0$ and $x = 0.55$ samples.

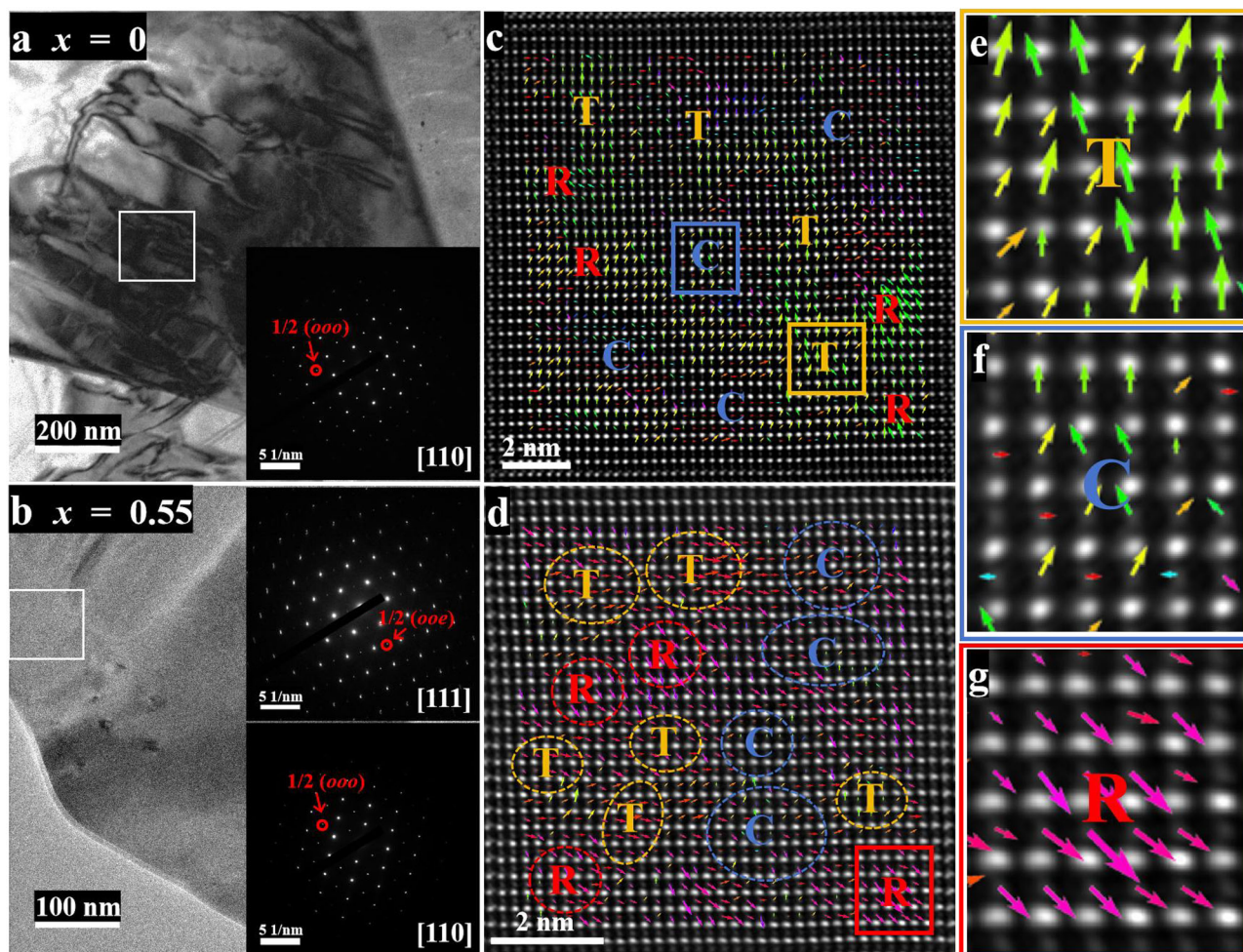


Fig. 2 | Local phase structure of the NBT and 0.55NBCSNLT samples. Bright-field TEM images of (a) NBT and (b) 0.55NBCSNLT, and the SAED patterns (insets) along $[110]_c$ of NBT and $[110]_c$, $[111]_c$ of 0.55NBCSNLT. c–g Atomic-resolution HAADF

images and the corresponding the cation displacement vectors along $[110]_c$ of 0.55NBCSNLT (dashed circles represent PNRs).

the long magnitude arrows, whereas the C phase shows near-zero polarization. It appears that the long-range ordered R-phase structure has been efficiently disrupted by the high entropy components with different ionic valence states, generating local T-phase and C-phase, which can also be clearly observed in Fig. 2c–g. Apparently, the captured image presents multiphase PNRs with R and T phases coexisting in the C matrix. Regions with the same polarization orientation form PNRs with sizes of 1–3 nm, verifying the coexistence of R-T-C multiphase PNRs in the macroscopic pseudo cubic phase^{27,28}. This disruption of long-range R-phase ordering is attributed to high-entropy-induced lattice distortions caused by mixed-valence cations, which promote localized T/C-phase nucleation, as confirmed by the atomic-scale structural evolution shown in Fig. 2c–g. The multiphase structure induced by the high entropy provides a basis for slim P - E loops and excellent ESP.

Energy storage performance of the x NBCSNLT samples

The P - E curves for all samples were tested under the electric field of their breakdown levels (Fig. S11). The E_b value was measured by Weibull distribution analysis as shown in Fig. S12. The pure NBT sample exhibits both large P_m and P_r , indicating a typical FE feature. Significantly narrowed P - E loops are observed in the x NBCSNLT samples, suggesting that the addition of NBCSNLT induces PNRs. Most importantly, the E_b monotonically increases as the NBCSNLT content (x) increases. The deduced P_m and E_b values were presented in Fig. 3a. It is observed that

the $P_m \cdot E_b$ relationship follows the paradox described by:

$$P_m = 99.912E_b^{-0.127} \quad (1)$$

The paradox holds for the E_b values below 550 kV/cm, beyond which it is broken. As a result, a significant enhancement of both P_m and E_b can be achieved simultaneously. The calculated values of W_{rec} and η are shown in Fig. S11. The W_{rec} value increases initially and then decreases with rising NBCSNLT content, reaching a record-high W_{rec} of 18.2 J/cm³ and a high η of 85.6% in the 0.55NBCSNLT sample. For the samples with $x > 0.55$, although E_b value continues to increase, the polarization strength ($\Delta P = P_m - P_r$), a key determinant of W_{rec} , deteriorates. This may be due to the presence of the nonpolar C phase, as shown in Fig. S8b, which dilutes the polar phase. Figure S13 shows the P_m , P_r , and η as a function of the NBCSNLT content. As the content of NBCSNLT increases, P_m initially decreases and then exhibits a peak at $x = 0.55$. P_r decreases rapidly in the range of $x \leq 0.35$ and reaches a very small value of 1.21 $\mu\text{C}/\text{cm}^2$ at $x = 0.35$. When $x > 0.35$, P_r is difficult to maintain at a low level but remains at a relatively high value. As x increases, ΔP registers a small and broad peak at $x = 0.35$ and a sharp peak at 0.55. The largest $\Delta P = 57.8 \mu\text{C}/\text{cm}^2$ is obtained in the 0.55NBCSNLT sample, which is 4.1 times that of pure sample (14.1 $\mu\text{C}/\text{cm}^2$). This finding, as well as the result in Fig. 3a, demonstrate that the superior ESP of the 0.55NBCSNLT sample is due to the

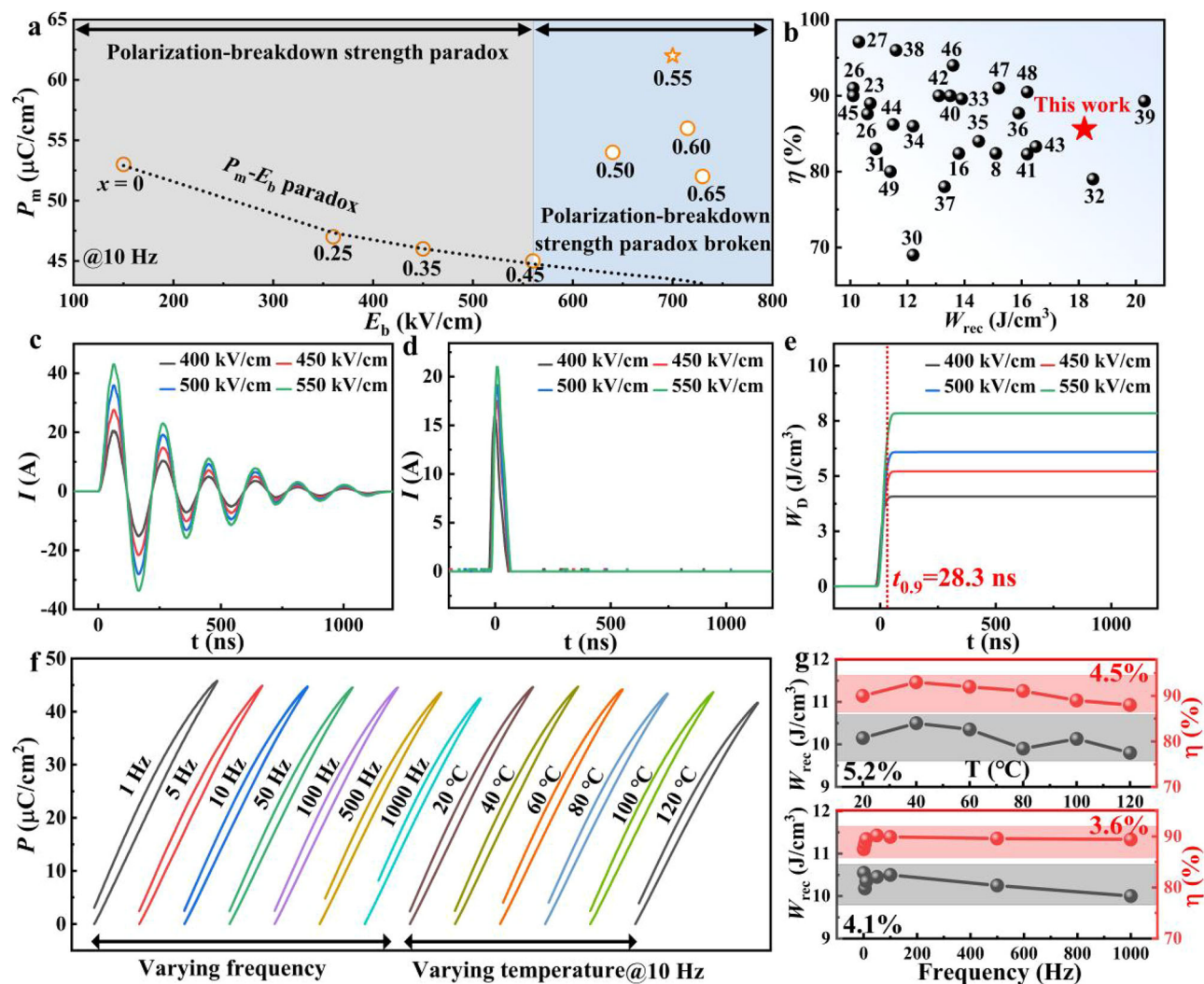


Fig. 3 | Energy storage performance of the xNBCSNLT samples. **a** P_m as a function of E_b for all the samples (The dotted line is the fitting curve based Eq. (1)). **b** W_{rec} and η of the 0.55NBCSNLT sample versus other energy storage ceramics with $W_{\text{rec}} \geq 10 \text{ J}/\text{cm}^3$. **c** Undamped charge and **d** over-damped discharge curves recorded

under various fields ranging from 400 to 550 kV/cm , **e** calculated W_d versus time of the 0.55NBCSNLT sample. **f** P - E loops under different temperatures and different frequencies of the 0.55NBCSNLT sample, and **g** the deduced W_{rec} and η as a function of temperature and frequency.

simultaneous improvement of P_m and E_b . The change in η is essentially the same as the change in ΔP . Therefore, the variations of P_m , P_r , and η with NBCSNLT content are not consistent. Figure 3b compares the ESP (W_{rec} and η) between the present sample and other lead-free ceramics with W_{rec} exceeding $10 \text{ J}/\text{cm}^3$ ^{16,23,26,27,29–49}. Among many lead-free energy storage ceramics, the highest W_{rec} value of $20.3 \text{ J}/\text{cm}^3$ was reported in $\text{Bi}_{0.5}\text{Na}_{0.5}\text{TiO}_3\text{-BaTiO}_3\text{-}0.1\text{Zn}_{1/3}\text{Nb}_{2/3}$ with a sample thickness of $\sim 50 \mu\text{m}$ ⁴². Although the W_{rec} value of the present sample ranks second, it is obtained in the sample with a thickness of $100 \mu\text{m}$. To make the W_{rec} values reported in the literature comparable, the energy-storage potential⁵⁰, defined as W_{rec}/E_b , is used. This parameter highlights the recoverable energy-storage density obtained per unit electric field. Since a smaller thickness results in a larger E_b , leading to a smaller W_{rec}/E_b value, this parameter mitigates the thickness effect, ensuring that the energy storage performance reported in different systems can be compared with each other. Figure S14 compares the W_{rec}/E_b as a function of E_b between the present sample and the latest lead-free energy storage ceramics with W_{rec} exceeding $10 \text{ J}/\text{cm}^3$, as tabulated in Table S2. Our sample shows a record high value of $W_{\text{rec}}/E_b = 0.026 \text{ mC}/\text{cm}^2$, which is of great importance for energy storage applications. Therefore, this sample is selected as a model for detailed investigations on charge-discharge properties. As shown in

Fig. 3c, d, the underdamped charge and overdamped discharge performances of the 0.55NBCSNLT sample were tested under different electric fields, respectively. Based on the first current peak amplitude (I_{max}) in Fig. 3c, the current density ($C_D = I_{\text{max}}/S$) and power density ($P_D = EI_{\text{max}}/2S$, where E is the electric field strength and S is electrode area) are calculated and plotted as a function of electric field in Fig. S15. At 550 kV/cm , the values of C_D and P_D are $1357 \text{ A}/\text{cm}^2$ and $373 \text{ MW}/\text{cm}^3$, respectively. Based on the discharge performance in Fig. 3d, the value of discharge energy density ($W_d = R\int i(t)^2 dt/V$) is calculated to be $8.2 \text{ J}/\text{cm}^3$. The sample exhibits an ultra-fast charge/discharge rate of $t_{0.9} = 28.3$ ns as seen in Fig. 3e. These parameters (C_D , P_D , and W_d) indicate that the 0.55NBCSNLT ceramic has excellent charge/discharge performance.

In practical applications, dielectric energy storage capacitors must be able to withstand harsh operating environments. Therefore, the frequency and temperature stabilities of the 0.55NBCSNLT sample were measured under 550 kV/cm . The results were shown in Fig. 3f, g. Over the wide temperature range of 20 – 120 °C, the variation rates of W_{rec} and η are only 5.2% and 4.5%, respectively. In the frequency range of 1 – 1000 Hz, the variation rates of W_{rec} and η are 4.1% and 3.6%, respectively. These values outperform many other excellent lead-free ceramics, demonstrating that the ESP of the 0.55NBCSNLT sample

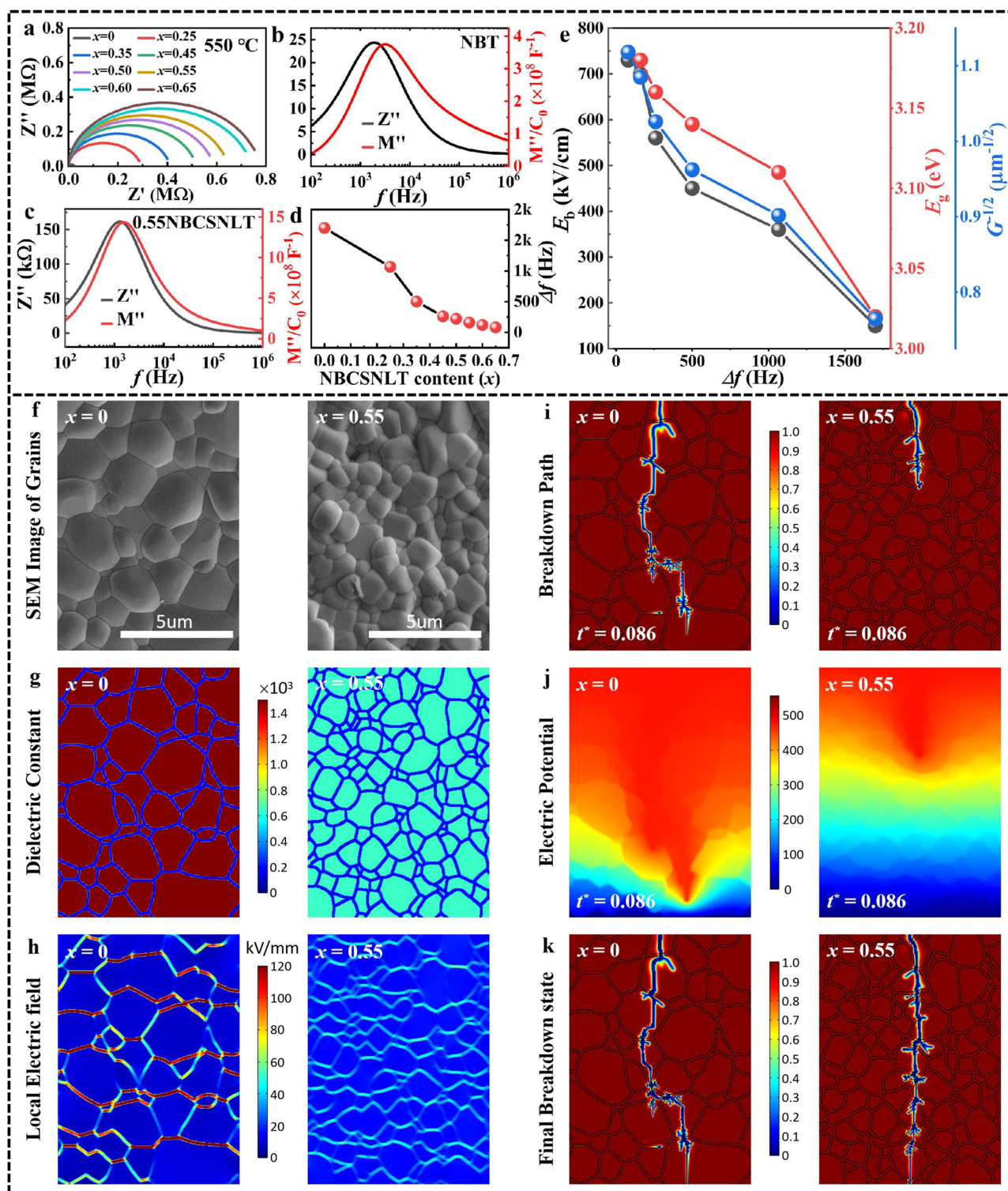


Fig. 4 | Evolution of interfacial polarization. **a** The complex impedance plots of all the samples. **b** and **c** The combined spectroscopic plots of Z'' and M'' recorded at 530 °C for the representative samples of NBT and 0.55NBCSNLT, respectively. **d** Δf as a function of x NBCSNLT content. **e** Curves of $G^{1/2}$, E_g , and E_b as a function of Δf .

f SEM images, **g** dielectric constant, **h** local electric field distributions, **i** breakdown path, **j** electric potential, **k** final breakdown state for the NBT and 0.55NBCSNLT samples.

possesses both excellent temperature stability and superior frequency stability.

Evaluation of interfacial polarization

Without exception, an ultrahigh W_{rec} ($>10 \text{ J/cm}^3$) is associated with an ultrahigh E_b value. Our previous study has shown that interfacial

polarization plays a vital role in determining E_b . To confirm this point, complex impedance plots at 550 °C were recorded in Fig. 4a. The complex impedance plot for samples with $x < 0.45$ shows a suppressed semicircle, indicating contributions from two adjacent semicircles (representing grains and grain boundaries). In contrast, the complex impedance plot for samples of $x > 0.45$ approximates an ideal

semicircle, indicative of a sole contribution (due to the suppression of interfacial polarization). Notably, the semicircle gradually enlarges as the x NBCSNLT increases, indicating that the leakage current density is effectively decreased by the NBCSNLT doping. This is directly proved by the result of leakage current density as a function of electric field, as shown in Fig. S16. The leakage current at room temperature (RT) and 100 kV/cm of the $x = 0.55$ sample is found to be 6.09×10^{-7} A/cm², which is much smaller than the that of the pure sample (7.85×10^{-7} A/cm²). Besides, the leakage current of both samples slightly increases as the measurement temperature increases from RT to 250 °C, indicating that the leakage current does not change significantly over the studied temperature range. The complex impedance plots can be well fitted by two R -CPE (R = resistor and CPE is constant phase element) circuits collected in series (Fig. S17a), with one representing the grain and the other representing the grain boundary. As an example, the comparison between experimental data and the fitting curves for samples of NBT and 0.55NBCSNLT samples was displayed in Fig. S17b. The fitting curves agree perfectly with the experimental data, indicating that satisfactory fits were achieved. The fitted values of grain resistance (R_g) and resistance mismatch $\Delta R = R_{gb} - R_g$ (R_{gb} being the grain boundary resistance) were presented as a function of the NBCSNLT content in Fig. S17c. As the NBCSNLT content increases, R_g significantly rises, while resistance mismatch rapidly decreases to zero. This result confirms that our high-entropy design can effectively reduce the resistance mismatch, thereby suppressing interfacial polarization. In order to confirm this point more visually, the Z'' - f and M'' - f spectra of the NBT and 0.55NBCSNLT recorded at 550 °C were illustrated in Fig. 4b, c, respectively. The spectra of other x NBCSNLT were shown in Fig. S18. As the NBCSNLT content increases, the Z'' and M'' peaks become closer and almost overlap when $x \geq 0.5$. Since the Z'' (M'') peak represents the contribution of the grain (grain boundary), the frequency gap (Δf) of the Z'' and M'' peaks actually reflects the strength of interfacial polarization⁵¹. When $\Delta f = 0$, i.e., the Z'' and M'' peaks appear at the same frequency, it indicates that the two R -CPE circuits are merged into one and interfacial polarization disappears. Figure 4d demonstrates that Δf decreases sharply and approaches zero with increasing x , reaching an extremely small value of 90 Hz in the $x = 0.65$ sample. This result confirms that the high-entropy design can effectively suppress the interfacial polarization.

It has been reported that the key parameters related to ESP, such as E_g , mean grain size (G), and E_b are closely related to the interfacial polarization⁹. The E_g values were measured by UV-vis absorption spectra as shown in Fig. S7. To estimate the mean grain size, scanning electron microscope (SEM) observations were conducted on all the samples in Fig. S19. The deduced G value, shown in Fig. S19, decreases with increasing the NBCSNLT content. Figure S20 shows the TEM surface morphology and energy-dispersive spectroscopy (EDS) mappings of the 0.55NBCSNLT ceramic, which reveals a dense structure and uniform distribution of elements. The relative density, which is the ratio of the experimental density measured by Archimedes' method to the theoretical density refined by Rietveld, is ranked in ascending order of NBCSNLT content as 89.5, 91.9, 92.3, 94.9, 96.2, 96.9, 97.3, and 98.1%. The obtained parameters of E_g , $G^{1/2}$, and E_b were plotted as a function of Δf , shown in Fig. 4e. Excitingly, all of them increase as Δf decreases. The most exciting finding is that the parameters show a sharp increase when Δf trends toward zero. This finding suggests that the physics behind these parameters might be the interfacial polarization. This naturally raises the question, since reducing grain size and interfacial polarization can both enhance E_b , which contributes significantly to enhancement of E_b ? In general, the grain size and E_b follow the empirical rule⁵² of $E_b = G^{1/2}$. Indeed, there is a good linear correlation between E_b and $G^{1/2}$ in samples with $x \leq 0.50$ ($R^2 = 0.998$). But for samples with $x > 0.50$, there is a significant increase in E_b (Fig. S21a). This enhancement can be ascribed to the reduction of interfacial polarization, as interfacial polarization tends to zero in these samples

(Fig. 4d). It is worth noting that Fig. S21b demonstrates a good linear relationship between relative density and breakdown strength. Another important question is whether the increase in E_b is caused by the increase in relative density? We believe that the increase in relative density and the decrease in interfacial polarization are essentially the same phenomenon. Due to the increase in relative density, the distinction between grains and grain boundaries gradually disappears, and interfacial polarization also diminishes, as clearly seen in Fig. S21c, because the space charges confined to grain boundaries no longer exist.

It is noteworthy that the high-entropy design not only promotes the above factors favorable for energy storage, but also significantly improves the temperature stability of dielectric constant and reduces the dielectric loss (Fig. S22). Compared with the pure sample, the 0.55NBCSNLT sample shows very a small dielectric loss tangent value (less than 5%) in the range of room temperature to 250 °C, indicating that the sample exhibits a minimal leakage current even at temperatures up to 250 °C. In addition the high-entropy design notably enhances the mechanical strength of the samples by reducing the electrostatic strain (Fig. S23). All these changes are helpful for boosting the ESP⁵³.

To clearly demonstrate that the interfacial polarization is suppressed by the high-entropy strategy, we quantitatively simulated the distributions of electric potential and local electric field of NBT and 0.55NBCSNLT samples under 100 kV/cm using the finite element method. The surface micrographs of both samples, shown in Figure 4f, were used as the basic structure for the simulation. To account for the significant decline in interfacial polarization with increasing x , the ratio of dielectric constants between grains and grain boundaries was adjusted from -1/10 to -1/5. The distributions of the dielectric constant, electric potential, and local electric field for NBT and 0.55NBCSNLT ceramics are presented sequentially in Fig. 4g–i. The simulation results clearly demonstrate that the dielectric constant of NBT shows a distinct difference between grains and grain boundaries. Meanwhile, the NBT sample has a high electric field at the grain boundaries, resulting in an uneven distribution of potential and local electric field. In contrast, the 0.55NBCSNLT sample exhibits uniform distribution of both electric field and potential, indicating the suppression of interfacial polarization. The result is directly confirmed by Kelvin probe force microscope (KPFM) observation, as shown in Fig. S24. From which, we can clearly see significant difference in surface potential between grains and grain boundaries for the NBT ($x = 0$) sample. In contrast, for the 0.55NBCSNLT sample, the surface potential distribution between the grains and grain boundaries is much more uniform. Since breakdown typically occurs where the local electric field is concentrated, a high E_b is expected in 0.55NBCSNLT.

To further corroborate this inference, a phase field model was employed to simulate the breakdown path with electric field increased from 0 to the E_b . The evolution of the breakdown path over time for NBT and 0.55NBCSNLT is shown in Fig. S25. Under E_b , the breakdown path starts at the top and rapidly passes through the NBT and 0.55NBCSNLT ceramics, with the dimensionless breakdown time, t^* , defined as the ratio of the actual time t to the characteristic time scale τ , found to be 0.086 and 0.092, respectively. Clearly, the 0.55NBCSNLT shows longer and more branched breakdown paths, correlating to the highest E_b . The final breakdown state of the NBT and 0.55NBCSNLT is shown in Fig. 4j, k, respectively. NBT reaches the breakdown state at $t^* = 0.086$, while 0.55NBCSNLT breaks down at $t^* = 0.092$. The t^* elongation of the 0.55NBCSNLT sample is due to the presence of a large number of grain boundaries, which effectively inhibit the growth of breakdown tips and slow down the development of breakdown paths. After comparing the breakdown process of two ceramics, it is clear that the breakdown path inside the 0.55NBCSNLT ceramic propagates slower than that of the NBT, with more derived branches. Thus, it is concluded that the 0.55NBCSNLT ceramic is more resistant

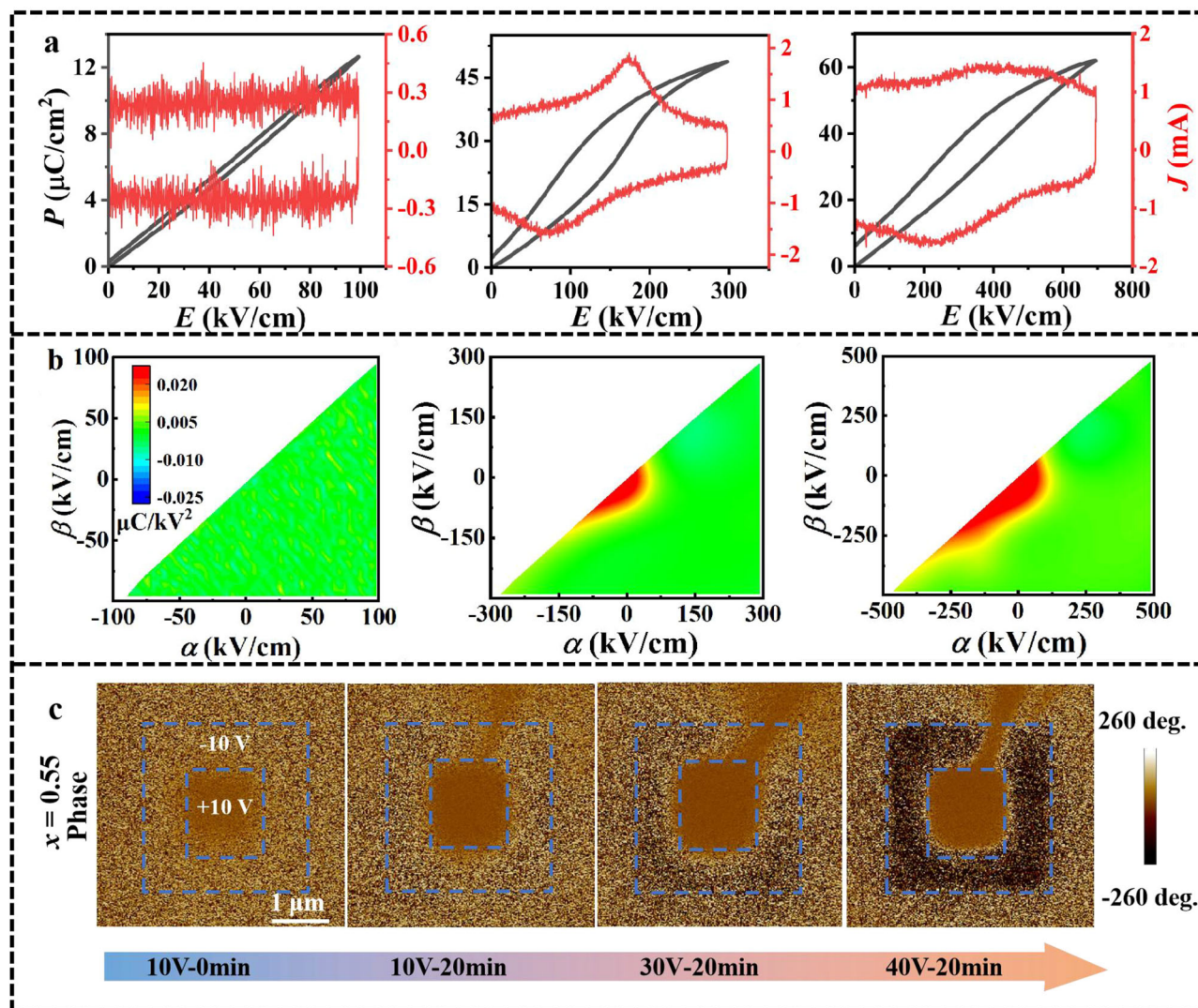


Fig. 5 | Electric-field-induced AFE to FE transition. **a** P - E and corresponding J - V loops under different electric fields, **b** FORC distributions under different electric fields of, and **c** PFM phase images under different voltages and dwell times of 0.55NBCSNLT ceramic.

to damage and exhibits significantly higher breakdown strength as compared to NBT.

Electric-field-induced AFE to FE transition

The above results clearly demonstrate that interfacial polarization was successfully suppressed by high entropy strategy. Resulting in a significant enhancement in E_b . To further understand the reason behind the enhancement of high-field polarization, the unipolar P - E loops of the 0.55NBCSNLT ceramic were tested in the range from 100 kV/cm up to 700 kV/cm, as shown in Fig. S26a. It is observed that polarization saturation is significantly delayed, likely due to clamping effects, and the E_b is markedly increased. The deduced W_{rec} as a function of E is plotted in Fig. S26b. The W_{rec} parabolically increases with the E up to 550 kV/cm, indicating that the sample behaves as linear dielectric material below 550 kV/cm. When $E > 550$ kV/cm, the data points for W_{rec} deviate from the parabolic trend, indicating that another polarization mechanism comes into play after the linear behavior. This field is termed the deviating field (E_d). It is noteworthy that the paradox is broken at a field just near E_d (Fig. 3a). This fact implies that it is the newly emerged polarization mechanism that enhances the polarization intensity, thereby breaking the paradox.

It is well-known that pure NBT exhibits FE R-phase ($R3c$) that changes to a weak AFE T-phase ($P4bm$) at temperatures above 320 °C⁵⁴.

The addition of NBCSNLT not only suppresses interfacial polarization but also alters the phase structure, as seen in Fig. S8b. The T-phase shifts to ambient temperature, and its content first increases and then decreases with the increase of NBCSNLT content due to the appearance of the C phase at high NBCSNLT levels. Consequently, the AFE feature, characterized by a pinched P - E loop, is initially obvious and then becomes less obvious, as confirmed in Fig. S11. The AFE phase is expected to transform into ferroelectric phase under a sufficiently high electric field, thereby greatly enhancing the polarization.

To clearly demonstrate the transitions of linear behavior to AFE phase and then to FE phase as the electric field increases, Fig. 5a shows the P - E loops and corresponding current density-voltage (J - V) loops of the 0.55NBCSNLT sample under three representative fields. At a low- E of 100 kV/cm, a slim P - E curve with negligible hysteresis area is accompanied by a square-shaped J - V loop. Both features indicate that the sample behaves as a nearly linear dielectric material. When E increases to a moderate field of 300 kV/cm, the P - E loop displays a pinched AFE nature with distinct current peaks in both forward and backward branches. This implies that the AFE nanodomains grow into microdomains and orient along the electric field direction, similar to FE polar nanoregions responding to external fields^{30,55}. These observations demonstrate that the AFE behavior appears alongside the linear behavior. However, as E increases to a high field of 700 kV/cm, both

the pinched AFE nature and the current peaks become less obvious. This result indicates that a high electric field transforms AFE to FE, resulting in a notable improvement in polarization from 48.7 to 62.1 $\mu\text{C}/\text{cm}^2$. Thus, the mechanism by which polarization is enhanced under high fields is the electric-field-induced AFE to FE transition.

First-order reversal curve (FORC) analysis was utilized to visualize the process of ferroelectric enhancement in the 0.55NBCSNLT sample with increasing electric field. Figure 5b shows the FORC plots recorded from three representative electric field ranges of -100 to 100 kV/cm, -300 to 300 kV/cm, and -500 to 500 kV/cm. In low- E range of -100 to 100 kV/cm, the homogeneous FORC distribution indicates linear polarization. In medium- E range of -300 to 300 kV/cm, a high-intensity region can be seen, which is significantly magnified in the high- E range of -500 to 500 kV/cm. High-intensity region represents strong nonlinear polarization. The FORC analysis demonstrates that ferroelectric domains are formed and ferroelectricity is enhanced as the electric field increases.

Besides the FORC analysis, the nanoscale domains in 0.55NBCSNLT can also be corroborated by the evolution law of domain structure (phase and amplitude) using piezoresponse force microscopy (PFM). Figure 5c compares PFM phase images of the 0.55NBCSNLT sample at different voltages (10 V/30 V/40 V) and dwell times (0 min/20 min). The domains of 0.55NBCSNLT ceramic can be observed at a voltage of 10 V within 20 min, which well explains the linear P - E curve of the 0.55NBCSNLT ceramic at low electric field (Fig. 5a). After being maintained at a voltage of 30 V for 20 minutes, a stable polarization response is excited, indicating relatively strong ferroelectricity with large P_m , high P_r , and notable hysteresis. Remarkably, under 40 V excitation, the domain structure with large P_m of the sample exhibits an enhanced inversion of the nonlinear polarization, demonstrating electric field-intensity-dependent ferroelectric activation. This threshold-driven behavior confirms the enhanced field-responsive configuration of polar nanoregions (PNRs) with adaptive phase boundaries in the 0.55NBCSNLT ceramic.

In conclusion, we proposed a method to break the P - E_b paradox for achieving outstanding ESP through a dedicated high entropy design to modulate both phase structure and interfacial polarization. These aims have been realized in NBCSNLT-modified NBT system, leading to the concurrent enhancement of both P and E_b . Accordingly, comprehensive ESP, including an ultrahigh W_{rec} of 18.2 J/cm³, a high η of 85.6%, a record high W_{rec}/E_b value of 0.026 mC/cm², superior thermal (20–120°C) and frequency (1–500 Hz) stabilities, was achieved in the bulk 0.45NBT-0.55NBCSNLT sample. This exceptional energy-storage performance was made possible by our unique high-entropy design, which effectively suppresses interfacial polarization. This suppression provides a sufficient electric field for the AFE-FE phase-transition, significantly boosting polarization. This work paves the way to overcome the polarization-breakdown strength paradox through a purpose-designed high entropy strategy, enabling the design of novel capacitors with superior ESP.

Methods

Sample preparation

The (1- x)NBT- x NBCSNLT ceramics were fabricated using a conventional solid-state reaction method. Na_2CO_3 (99%), Bi_2O_3 (99%), CaCO_3 (99%), SrCO_3 (99.99%), Nd_2O_3 (99.99%), Li_2CO_3 (99.99%), and TiO_2 (99%) were accurately calculated. The weighed materials milled with alcohol and zirconia beads at 400 rpm for 16 h. The dried mixed powder was calcined at 900°C for 6 h. The calcined samples were reground to powder and ball milled again for 16 h. The powder was bound by 6% PVA and pressed under a pressure of 10 Mpa to form a cylinder. The pellets were sintered at 1190 °C for 2 h.

Electrical property measurements

The P - E and S - E loops were measured using ferroelectric hysteresis measurement tester (Precision multiferroelectric, Radiant Technologies

Inc, NM) with the sample thickness of 0.12 mm. Gold electrodes with a diameter of 1 mm were sputtered onto the surface of the polished sample. The underdamped and overdamped charge-discharge performance of the 0.55NBCSNLT ceramic was tested using a charge-discharge performance test system (Guoguo, CFD-005) with a sample thickness of 0.12 mm, a gold electrode diameter of 2 mm, and an external load resistance was 200 Ω . The dielectric and impedance properties were tested by Wayne Kerr 6500B impedance analyzer (Wayne Kerr Electronic Instrument Co., Shenzhen, China) with silver electrodes pasted on both sides of the polished samples.

Calculations and simulations

A detailed description of the calculation process, including the Density function theory (DFT) calculations, FORC, finite element simulation, and phase field simulation, is also available in the Supporting Information.

Characterization

The crystal structure of all the samples was measured by X-ray diffraction at room temperature. Rietveld refinements were collected through the GSAS software. Synchrotron XRD experimental ($\lambda = 0.77485$ Å) data were collected at the Australian Synchrotron Beamline. The optical absorption and diffuse reflection properties of the particle sample were examined with a UV-vis spectrophotometer (Lambda 1050, USA). The ceramics were cut into 10 μm slices using Carl Zeiss Crossbeam 550 L focused ion beam (FIB) and then tested under the JEOL JEM-2100 instrument for bright field TEM, SAED, and EDS. High-angle annular dark-field scanning transmission electron microscopy (HAADF-STEM) characterization was performed using two aberration-corrected instruments: a JEOL ARM 200 CFEG-STEM with a probe-forming spherical aberration corrector operating at 200 kV, and an FEI Titan Themis Z microscope equipped with dual probe aberration correctors operating at 300 kV. The surface morphology of the samples was examined using a field emission scanning electron microscope (FE-SEM, Regulus 8230, Hitachi Co., Tokyo, Japan) on polished and thermally etched surfaces. The surface potential distribution was tested using a Kelvin Probe Force Microscope (KPFM, Hitachi 5500 m). The domain structure of ceramic samples was analyzed using PFM (Bruker Dimension Icon).

Data availability

All data supporting this study and its findings are available within the article and its Supplementary Information. Any data deemed relevant is available from the corresponding author upon request.

References

1. Yang, L. et al. Perovskite lead-free dielectrics for energy storage applications. *Prog. Mater. Sci.* **102**, 72–108 (2019).
2. McPherson, J. et al. Trends in the ultimate breakdown strength of high dielectric-constant materials. *IEEE Transact. Electron. Dev.* **50**, 1771–1777 (2003).
3. Wu, L. et al. Enhanced energy density in core-shell ferroelectric ceramics: Modeling and practical conclusions. *J. Am. Ceram. Soc.* **99**, 930–937 (2015).
4. Cai, Z. et al. Giant dielectric breakdown strength together with ultrahigh energy density in ferroelectric bulk ceramics via layer-by-layer engineering. *J. Mater. Chem. A* **7**, 17283–17291 (2019).
5. Yan, F. et al. Composition and structure optimized BiFeO₃-SrTiO₃ lead-free ceramics with ultrahigh energy storage performance. *Small* **18**, 2106515 (2022).
6. Wang, H. et al. Ultrahigh energy-storage density in antiferroelectric ceramics with field-induced multiphase transitions. *Adv. Funct. Mater.* **29**, 1807321 (2019).
7. Guo, Y. et al. Dynamic hysteresis scaling of ferroelectric Pb_{0.9}Ba_{0.1}(Zr_{0.52}Ti_{0.48})O₃ thin films. *J. Phys. Condens. Matter* **21**, 485901 (2009).

8. Cao, W. et al. Interfacial Polarization restriction for ultrahigh energy storage density in lead-free ceramics. *Adv. Funct. Mater.* **33**, 2301027 (2023).
9. Zhao, H. et al. Suppressing interfacial polarization via entropy increase strategy for superior energy-storage performance of $\text{Na}_{0.5}\text{Bi}_{0.5}\text{TiO}_3$ -based ceramics. *J. Mater.* **10**, 947–955 (2024).
10. Zhao, H. et al. Lead-free medium-entropy $(\text{Na}_{0.47(1-x)}\text{Bi}_{0.47(1-x)}\text{Ba}_{0.06(1-x)}\text{Sr}_{0.7x}\text{Nd}_{0.2x})\text{TiO}_3$ relaxor ceramics with robust energy-storage performance. *Chem. Eng. J.* **471**, 144702 (2023).
11. Mendez-González, Y. et al. Effect of the lanthanum concentration on the physical properties of the $(\text{Bi}_{0.5}\text{Na}_{0.5})_{0.92}\text{Ba}_{0.08-3x/2}\text{La}_x\text{TiO}_3$ ceramic system. *Mater. Chem. Phys.* **208**, 103–111 (2018).
12. Che, Z. et al. Phase structure and defect engineering in $(\text{Bi}_{0.5}\text{Na}_{0.5})\text{TiO}_3$ -based relaxor antiferroelectrics toward excellent energy storage performance. *Nano Energy* **100**, 107484 (2022).
13. Qin, M. et al. Point defect structure of La-doped SrTiO_3 ceramics with colossal permittivity. *Acta Mater.* **164**, 76–89 (2019).
14. Li, X. et al. Realizing high energy density and efficiency simultaneously in $(\text{Bi}_{0.5}\text{Na}_{0.5})_{0.7}\text{Sr}_{0.3}\text{TiO}_3$ -based ceramics via introducing linear dielectric CaTiO_3 . *J. Mater. Chem. A* **10**, 18343–18353 (2022).
15. Antoinette, M. et al. Experimental charge density distribution and its correlation to structural and optical properties of Sm^{3+} doped Nd_2O_3 nanophosphors. *J. Rare. Earth* **35**, 1102–1114 (2017).
16. Perdew, J. et al. Generalized gradient approximation made simple. *Phys. Rev. Lett.* **77**, 3865 (1998).
17. Yang, B. et al. Engineering relaxors by entropy for high energy storage performance. *Nat. Energy* **8**, 956–964 (2023).
18. Tang, L. et al. Giant energy storage density with antiferroelectric-like properties in BNT-based ceramics via phase structure engineering. *Small* **19**, 2302346 (2023).
19. Cao, W. et al. Boosting energy-storage performance in lead-free ceramics via polyphase engineering in the superparaelectric state. *Compos Part B Eng.* **255**, 110630 (2023).
20. Shi, W. et al. Moderate fields, maximum potential: Achieving high records with temperature-stable energy storage in lead-free BNT-based ceramics. *Nano-Micro Lett.* **16**, 91 (2023).
21. Li, T. et al. High-performance strain of lead-free relaxor-ferroelectric piezoceramics by the morphotropic phase boundary modification. *Adv. Funct. Mater.* **32**, 2202307 (2022).
22. Lv, Z. et al. NaNbO_3 -based multilayer ceramic capacitors with ultrahigh energy storage performance. *Adv. Energy Mater.* **14**, 2304291 (2024).
23. Guo, J. et al. Multi-symmetry high-entropy relaxor ferroelectric with giant capacitive energy storage. *Nano Energy* **112**, 108458 (2023).
24. Wang, W. et al. Enhanced energy storage properties in lead-free $(\text{Na}_{0.5}\text{Bi}_{0.5})_{0.7}\text{Sr}_{0.3}\text{TiO}_3$ -based relaxor ferroelectric ceramics through a cooperative optimization strategy. *ACS Appl. Mater. Interfaces* **15**, 6990–7001 (2023).
25. Shi, T. et al. Remarkably minimized domain and elevated energy storage properties in $\text{Na}_{0.48}\text{Bi}_{0.48}\text{Ba}_{0.04}\text{TiO}_3$ -based relaxor antiferroelectrics by interposing $\text{Bi}(\text{Mg}_{2/3}\text{Ta}_{1/3})\text{O}_3$. *Chem. Eng. J.* **470**, 144205 (2023).
26. Chen, L. et al. Local Diverse polarization optimized comprehensive energy-storage performance in lead-free superparaelectrics. *Adv. Mater.* **34**, 2205787 (2022).
27. Li, D. et al. A high-temperature performing and near-zero energy loss lead-free ceramic capacitor. *Energy Environ. Sci.* **16**, 4511 (2023).
28. Zhao, W. et al. Broad-high operating temperature range and enhanced energy storage performances in lead-free ferroelectrics. *Nat. Commun.* **14**, 5725 (2023).
29. Chen, L. et al. Giant energy-storage density with ultrahigh efficiency in lead-free relaxors via high-entropy design. *Nat. Commun.* **13**, 3089 (2022).
30. Qi, H. et al. Ultrahigh energy-storage density in NaNbO_3 -based lead-free relaxor antiferroelectric ceramics with nanoscale domains. *Adv. Funct. Mater.* **29**, 1903877 (2019).
31. Jiang, J. et al. Enhanced energy storage properties of lead-free NaNbO_3 -based ceramics via A/B-site substitution. *Chem. Eng. J.* **422**, 130130 (2021).
32. Jiang, J. et al. Ultrahigh energy storage density in lead-free relaxor antiferroelectric ceramics via domain engineering. *Energy Storage Mater.* **43**, 383–390 (2021).
33. Cui, T. et al. Simultaneous achievement of ultrahigh energy storage density and high efficiency in BiFeO_3 -based relaxor ferroelectric ceramics via a highly disordered multicomponent design. *J. Mater. Chem. A* **10**, 14316–14325 (2022).
34. He, B. et al. Excellent energy storage performance of $(\text{Sc}_{0.5}\text{Ta}_{0.5})^{4+}$ modified $(\text{Bi}_{0.5}\text{Na}_{0.5})\text{TiO}_3$ -based ceramics modulated by the evolution of polar Phases. *J. Mater. Chem. A* **11**, 14169–14179 (2023).
35. Pan, T. et al. Enhanced energy density and efficiency in lead-free sodium niobate-based relaxor antiferroelectric ceramics for electrostatic energy storage application. *Adv. Electron. Mater.* **8**, 2200793 (2022).
36. Cui, T. et al. Outstanding comprehensive energy storage performance in lead-free BiFeO_3 -based relaxor ferroelectric ceramics by multiple optimization Design. *Acta Mater.* **240**, 118286 (2022).
37. Wu, J. et al. High energy storage performance in BiFeO_3 -based lead-free high-entropy ferroelectrics. *Small* **240**, 2400997 (2024).
38. Chen, L. et al. Near-zero energy consumption capacitors by controlling inhomogeneous polarization configuration. *Adv. Mater.* **36**, 2313285 (2024).
39. Sun, Z. et al. Strong local polarization fluctuations enabled high electrostatic energy storage in Pb-free relaxors. *J. Am. Chem. Soc.* **146**, 13467–13476 (2024).
40. Guan, Z. et al. Significantly enhanced energy storage performance of lead-free BiFeO_3 -based ceramics via synergic optimization strategy. *ACS Appl. Mater. Interfaces* **14**, 44539–44549 (2022).
41. Ma, J. et al. Achieving ultrahigh energy storage density in lead-free sodium niobate-based ceramics by modulating the antiferroelectric phase. *Chem. Mater.* **34**, 7313–7322 (2022).
42. Xie, A. et al. Supercritical relaxor nanograined ferroelectrics for ultrahigh-energy-storage capacitors. *Adv. Mater.* **34**, 2204356 (2022).
43. Jiang, J. et al. Novel lead-free NaNbO_3 -based relaxor antiferroelectric ceramics with ultrahigh energy storage density and high efficiency. *J. Mater.* **8**, 295–301 (2022).
44. Pan, T. et al. Improved capacitive energy storage in sodium niobate-based relaxor antiferroelectric ceramics. *Appl. Phys. Lett.* **122**, 072902 (2023).
45. Sun, Z. et al. Superior capacitive energy-storage performance in Pb-free relaxors with a simple chemical composition. *J. Am. Chem. Soc.* **145**, 6194 (2023).
46. Liu, H. et al. Chemical design of Pb-free relaxors for giant capacitive energy storage. *J. Am. Chem. Soc.* **145**, 11764 (2023).
47. Liu, H. et al. Local chemical clustering enabled ultrahigh capacitive energy storage in Pb-free relaxors. *J. Am. Chem. Soc.* **145**, 19396 (2023).
48. Luo, H. et al. Outstanding energy-storage density together with efficiency of above 90% via local structure design. *J. Am. Chem. Soc.* **146**, 460 (2024).
49. Chen, L. et al. Compromise optimized superior energy storage performance in lead-free antiferroelectrics by antiferroelectricity modulation and nanodomain engineering. *Small* **20**, 2306486 (2024).
50. Gao, Y. et al. Grain size modulated $(\text{Na}_{0.5}\text{Bi}_{0.5})_{0.65}\text{Sr}_{0.35}\text{TiO}_3$ -based ceramics with enhanced energy storage properties. *Chem. Eng. J.* **433**, 133584 (2022).

51. Cao, W. J. et al. Interfacial-polarization engineering in BNT-based bulk ceramics for ultrahigh energy-storage density. *Adv. Sci.* **11**, 2409113 (2024).
52. Young, A. et al. Effect of liquid-phase sintering on the breakdown strength of barium titanate. *J. Am. Ceram. Soc.* **90**, 1504–1510 (2007).
53. Wang, L. et al. Excellent energy-storage performance in BNT-BT lead-free ceramics through optimized electromechanical breakdown. *Mater. Today Phys.* **47**, 101545 (2024).
54. Yin, J. et al. Nanoscale bubble domains with polar topologies in bulk ferroelectrics. *Nat. Commun.* **12**, 3632 (2021).
55. Qi, H. et al. Giant electrostrictive strain in $(\text{Bi}_{0.5}\text{Na}_{0.5})\text{TiO}_3\text{-NaNbO}_3$ lead-free relaxor antiferroelectrics featuring temperature and frequency stability. *J. Mater. Chem. A* **8**, 2369 (2020).

Acknowledgements

The work was supported by the National Natural Science Foundation of China (Grant Nos. 12174001 and No. 12402190). Xu Hou also would like to acknowledge the fellowship award from the Research Grants Council of the Hong Kong Special Administrative Region, China (Project No. PolyU PDFS2223-5S08) and the PolyU Distinguished Postdoctoral Fellowship Scheme (No. 1-YWBC) for the kind support.

Author contributions

This work was conceived and designed by Wenjun Cao, Chunchang Wang and Zhenxiang Cheng conceived the idea. Sample fabrication was performed by Wenjun Cao, Xuecen Huang, Feng Li, and Youmin Guo, who also conducted XRD, energy storage, dielectric, UV-Vis, and charge-discharge performance tests, as well as analyzed relevant data. Daqin Guan and Zhenxiang Cheng carried out synchrotron X-ray measurements and data analysis. Finite element simulations of breakdown characteristics were conducted by Xu Hou. Yanwei Wu conducted theoretical calculations and analysis. SEM, TEM, and HAADF-STEM imaging were carried out by Wenjun Cao, Xiaoyu Yang, and Binghui Ge and processed accordingly. All authors participated in data analysis and discussions.

Competing interests

The authors declare no competing interests.

Additional information

Supplementary information The online version contains supplementary material available at <https://doi.org/10.1038/s41467-025-61030-7>.

Correspondence and requests for materials should be addressed to Chunchang Wang, Binghui Ge, Xu Hou or Zhenxiang Cheng.

Peer review information *Nature Communications* thanks Priyanka A. Jha, Maqbool Ur Rehman, and the other anonymous reviewer(s) for their contribution to the peer review of this work. A peer review file is available.

Reprints and permissions information is available at <http://www.nature.com/reprints>

Publisher's note Springer Nature remains neutral with regard to jurisdictional claims in published maps and institutional affiliations.

Open Access This article is licensed under a Creative Commons Attribution-NonCommercial-NoDerivatives 4.0 International License, which permits any non-commercial use, sharing, distribution and reproduction in any medium or format, as long as you give appropriate credit to the original author(s) and the source, provide a link to the Creative Commons licence, and indicate if you modified the licensed material. You do not have permission under this licence to share adapted material derived from this article or parts of it. The images or other third party material in this article are included in the article's Creative Commons licence, unless indicated otherwise in a credit line to the material. If material is not included in the article's Creative Commons licence and your intended use is not permitted by statutory regulation or exceeds the permitted use, you will need to obtain permission directly from the copyright holder. To view a copy of this licence, visit <http://creativecommons.org/licenses/by-nc-nd/4.0/>.

© The Author(s) 2025